Tellus (1989), *41A*, 73–96

Model simulations of the M_2 and the K_1 tide in the Nordic Seas and the Arctic Ocean

By B. GJEVIK and T. STRAUME, *Institute of Mathematics, University of Oslo, P.O. Box 1053, Blindern, Norway*

(Manuscript received 9 September 1987; in final form 22 April 1988)

ABSTRACT

The depth-integrated tidal equations have been solved numerically for a model basin covering the North Sea and the Norwegian–Greenland–Barents Seas and the Arctic Ocean. The model is implemented on a stereographic map projection with a grid size 50 × 50 km at 60° N. The semi-diurnal M_2 component and the diurnal K_1 component have been simulated. Correlation coefficients between computed and measured M_2 and K_1 amplitudes for 116 tidal stations located all around the Nordic Seas were found to be 0.97 and 0.82, respectively. The standard deviation for the corresponding linear regression analysis is ± 0.12 m and ± 0.02 m, respectively. For the continental shelf along the western coast of Norway and the Barents Sea, the performance of the model is particularly good and the values for the correlation coefficients and standard deviations for this region are 0.97, 0.92, ± 0.09 m and ± 0.03 m.

The M_2 tide is mainly a co-oscillating tide driven by energy influx from the North Atlantic. The K_1 tide is strongly affected by the direct effect of the tide-generating force particularly in the North Sea region and along the coast of western Norway.

Different forms of boundary condition along the open boundary towards the North Atlantic have been implemented and tested by comparing the results of the simulation with measurements. Co-range and co-tidal charts are presented and the regional variation of the tidal currents is displayed by maps showing the principal axis of current ellipse and the sense of rotation of the current vector. Energy fluxes are computed for key sections within the model basin and a tidal energy budget for the main parts of the basins is given.

1. Introduction

The Arctic Ocean and the adjacent Nordic Seas, i.e., the Norwegian–Greenland–Barents Seas and the North Sea, form an interconnected ocean system. It interacts with the world ocean through the main passages towards the North Atlantic between Scotland, the Faeroes, Iceland and Greenland. The tide in this ocean system was not resolved well by the large-scale global models by Zahel (1975) and Hendershott (1977). New progress in global modelling was made by Schwiderski (1980a, b) with the introduction of a unique method which combined model simulation and empirical data. This led to global tidal charts with a substantially finer resolution and a higher degree of accuracy. The tidal elevation in the Nordic Seas was computed on a 1° by 1° grid system and the results are generally in good agreement with observations (Schwiderski, 1986). Important details especially in the region near the Shetlands and the Faeroes and also in the Barents Sea may however not be resolved well by Schwiderski's model.

Regional models with fine spatial resolution have also been used extensively for modelling the tide in the North Sea and the northeast Atlantic (Hansen, 1949; Flather, 1976, 1981; Davies and Furnes, 1980; Mathisen and Johansen, 1983; Flather et al., 1987). Moreover, a regional model for the Arctic Ocean has been developed by Kowalik and Untersteiner (1978) and Kowalik (1979). In regional models the tide-generating force is generally neglected and the tidal motion is driven as a co-oscillating tide by specifying the motion along the open ocean boundaries of the model. The North Sea and the northeast Atlantic continental shelf models have open boundaries towards the North Atlantic west of Ireland and towards the Norwegian Sea south of the 65° N latitude. In the large northeast Atlantic model (Flather, 1981; Flather et al., 1987), the open boundary to the north is located in the Norwegian–Greenland Sea at about 72° N and the open boundary to the west is in the Atlantic Ocean along the 30° W longitude. For this large regional model, Flather et al. (1976) also investigated the effect of the tide generating force. The model developed by Kowalik and Untersteiner (1978) for the semi diurnal tide in the Arctic Ocean has its open boundary in the Norwegian–Greenland Seas between 67° N and 70° N. Despite the extensive amount of information provided by all these models, the details of the tides particularly in the northern area of the Nordic Seas may still not be well resolved and the complete structure of tidal interaction with the Arctic Ocean remains to be investigated. For tidal modelling for example along the western and northern coast of Norway, where the interaction between Arctic Ocean and the Norwegian and the Barents Seas is particularly important, a new large-scale model with open boundaries far away from the area of interest is clearly required. We have therefore implemented a tidal model which covers the ocean system formed by the Arctic Ocean and the Nordic Seas. This model has mainly coastal boundaries except for the open boundary in the north Atlantic Ocean along a line from Ireland to Greenland south of Iceland and in the narrow Irish Sea and the English Channel. In this first part of the study, we shall focus on the tidal motion in the northern region of Nordic Seas rather than the finer details of the tide in the Arctic Ocean. The tidal interaction through the narrow Bering Strait and the straits between Greenland and the islands north of Canada has therefore been ignored. The grid representation of the model area is shown in Fig. 1 and a map of the bathymetry of the main model area can be found in Gjevik (1988).

In this study, we have also neglected the effect of the polar sea ice on the tide. The ice will certainly lead to an enhancement of energy dissi-

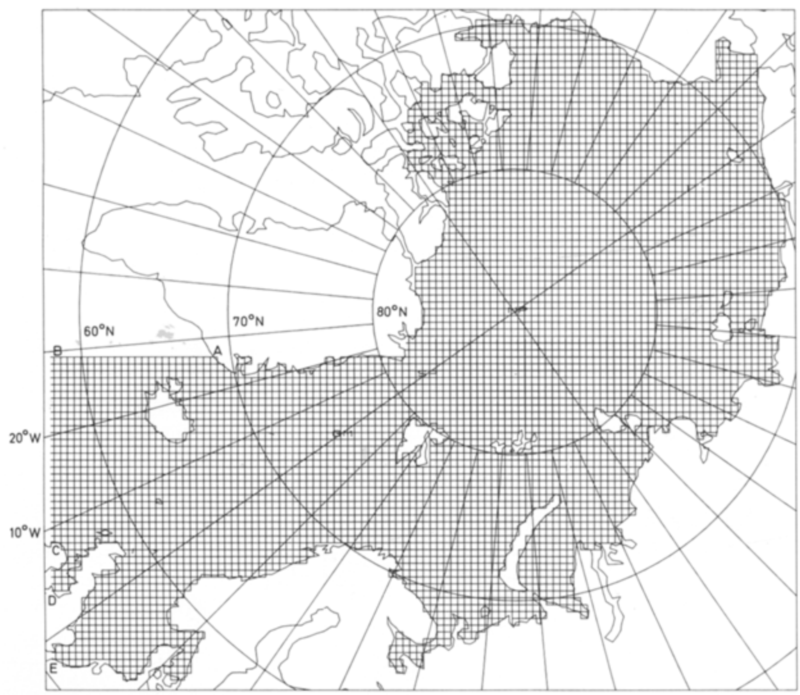

Fig. 1. Grid representation of model area. Grid size 50 km at 60° N. Open boundaries at A–B–C, D and E.

pation due to the induced straining and cracking of the ice floes. The effect will most likely be strongest in regions where the divergence of the tidal flow is large and causing periodic opening and closing of the ice cover. Kowalik and Untersteiner (1978) found the largest values of the divergence were confined to the shallow water of the Eurasian shelf. The additional friction may however only have a minor effect on the amplitude of the tide in the deeper part of the Arctic Ocean. This is also confirmed by the results of a study of the effect of the ice-cover on the M_2 tide in the Arctic Ocean by Kowalik (1981).

Due to the large extent of the region covered by the model the direct tide generated by the action of the tidal force on the water mass within the region may not be negligible. The model simulation for the K_1 tidal component shows that the tidal force have an important effect on the diurnal tide. For the M_2 semi-diurnal tide, the effect of the tidal force is small and we find that the semi-diurnal tide within the model area mainly is a co-oscillating tide propagating into the Norwegian and Greenland Seas from the North Atlantic. The wave proceeds into the Barents Sea and the Arctic Ocean and leads to a net northward energy flux both in the Fram Strait and in the passages between Spitsbergen–Franz Josef Land–Severnaya Zemlya. This agrees well with the results of Schwiderski (1986), but there are some important differences with respect to the structure of the tidal motion in local areas. For example, this model does show a well-developed amphidrome for the semi-diurnal M_2 tide in the Barents Sea southeast of Spitsbergen. This agrees well with early empirical and computed tidal maps by Nekrasov (1961, 1962) while the map by Schwiderski (1986) only displays an incomplete amphidrome in this region.

For the northern region covered by the model, there is a notable shortage of pelagic tidal data. The IAPSO publication on pelagic tidal constants (Cartwright and Zetler, 1985) does not include any references to pelagic measurements in the Arctic Ocean, the Barents Sea and the northern parts of the Norwegian–Greenland Seas. Comparison with observations for this part of the

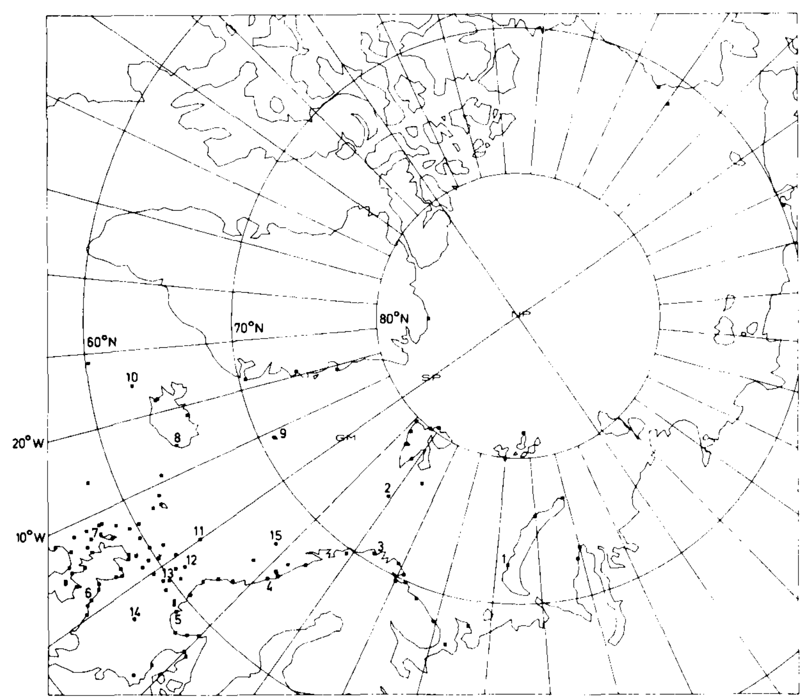

Fig. 2. Position of 116 tidal stations (mark □) used for comparison of measured and computed harmonic constants. Station numbers correspond to list in Tables 1, 6.

model area therefore has to rely mainly on coastal tidal data. For the southern part of the model area, there is a considerable amount of pelagic data available especially in the North Sea and in the Shetland–Faeroe regions. In addition there is a large number of coastal stations with tidal constants determined from long tidal records. We have made direct comparison between model predictions and observations for the M_2 and K_1 components for a selection of 116 different stations located all around the Nordic Seas but with a denser concentration in the area north of the British islands and along the Norwegian coast (Fig. 2). Of this total number there is 27 pelagic tidal stations. The detailed results of this extensive comparison between model and observational tidal constants are reported in Sections 5, 6.

2. Basic equations

We shall use the linearized depth averaged tidal equation which in a spherical coordinate system reads

$$\frac{\partial u_\theta}{\partial t} - f u_\phi = -\frac{g}{R\cos\phi}\frac{\partial}{\partial\theta}(\eta - \bar{\eta}) + A_\theta + B_\theta, \quad (2.1)$$

$$\frac{\partial u_\phi}{\partial t} + f u_\theta = -\frac{g}{R}\frac{\partial}{\partial\phi}(\eta - \bar{\eta}) + A_\phi + B_\phi, \quad (2.2)$$

$$\frac{\partial \eta}{\partial t} = -\frac{1}{R\cos\phi}\left[\frac{\partial}{\partial\theta}(u_\theta h) + \frac{\partial}{\partial\phi}(u_\phi h\cos\phi)\right]. \quad (2.3)$$

Here, ϕ and θ denote geographical latitude and longitude, respectively, u_ϕ and u_θ are the corresponding northward and eastward mean current velocity and t denotes time. The undisturbed depth of the ocean is h, η is the displacement of the sea surface from its undisturbed position and $\bar{\eta}$ is the equilibrium tide or the astronomic tide-generating potential. Deformation of the earth by the direct effect of tidal forces are accounted for by the body tide correction factor in the potential (see Appendix). The mean radius of the earth is denoted by R, the Coriolis parameter $f = 2\Omega\sin\phi$ where Ω is the angular velocity of the earth and g is the acceleration due to gravity. The vector components (A_θ, A_ϕ) and (B_θ, B_ϕ) denote the bottom shear stress and the lateral friction per unit mass respectively.

A stereographic map projection is introduced in order to avoid the singularity in eqs. (2.1) and (2.3) at the pole ($\phi = \pi/2$). This also has the advantages that the numerical computations can be performed on a grid where each grid box covers approximately the same area. We define a Cartesian coordinate system (x, y) with origin at the axis of rotation of the earth and the x-axis in the direction of a meridian θ_0. Hence,

$$x = r\cos\hat{\theta},$$

$$y = r\sin\hat{\theta},$$

where $\hat{\theta} = \theta - \theta_0$ and

$$r = aR\cos\phi.$$

The scaling factor is

$$a = \frac{1 + \sin\phi_0}{1 + \sin\phi}, \quad (2.4)$$

where ϕ_0 is the latitude through which the plane of the stereographic projection passes. For numerical computations, it is convenient to express the scaling factor by the distance r measured on the map. If the scale of the map is a_s at a latitude $\phi = \phi_s$ corresponding to $r = r_s$ and the distance from the pole to the equator (measured on the map) is r_0 we have

$$m = \frac{a}{a_s} = \frac{r^2 + r_0^2}{r_s^2 + r_0^2}, \quad (2.5)$$

where m is the map factor.

With $m = 1$ for $\phi_s = 60°$, the variation of m within the model area range from 0.93 at the pole to 1.06 at the southern boundary of the model.

By transforming from geographical coordinates (ϕ, θ) to Cartesian coordinates (x, y), the depth integrated tidal equations (2.1) and (2.2) can be written

$$\frac{\partial U}{\partial t} - fV = -mgh\frac{\partial}{\partial x}(\eta - \bar{\eta}) + A_x + B_x, \quad (2.6)$$

$$\frac{\partial V}{\partial t} + fU = -mgh\frac{\partial}{\partial y}(\eta - \bar{\eta}) + A_y + B_y, \quad (2.7)$$

and the continuity equation (2.3) reads

$$\frac{\partial \eta}{\partial t} = -m^2\left[\frac{\partial}{\partial x}\left(\frac{U}{m}\right) + \frac{\partial}{\partial y}\left(\frac{V}{m}\right)\right]. \quad (2.8)$$

The volume fluxes in the x- and y-directions are defined by

$$U = -h(u_\phi\cos\hat{\theta} + u_\theta\sin\hat{\theta}), \quad (2.9)$$

$$V = h(-u_\phi \sin\hat{\theta} + u_\theta \cos\hat{\theta}), \tag{2.10}$$

respectively. The x- and y-components of the bottom stress (A_x, A_y) and the lateral friction force (B_x, B_y) are obtained by a similar transformation as for the volume flux vector (eqs. 2.9 and 2.10). It should be noted that (2.8) is an exact form of the continuity equation. Kowalik and Untersteiner (1978) also used a stereographic map projection for their model of the Arctic Ocean but with an approximate form of the continuity equation. This approximation is valid provided

$$\left|\frac{1}{U}\frac{\partial U}{\partial x}\right| \gg \left|\frac{1}{m}\frac{\partial m}{\partial x}\right|$$

with a similar requirement for V.

We shall parameterize the bottom stress vector (A_x, A_y) by

$$A_x = -kU/h, \tag{2.11}$$

$$A_y = -kV/h, \tag{2.12}$$

where k is the bottom friction coefficient. By choosing

$$k = c_f(U^2 + V^2)^{\frac{1}{2}}/h, \tag{2.13}$$

where c_f is a drag coefficient, this corresponds to a quadratic bottom friction law which has been used frequently in tidal models (Schwiderski, 1980a). The drag coefficient c_f is typically of order $3 \cdot 10^{-3}$.

The quadratic friction law leads to nonlinear interaction between tidal constituents with different frequencies. A strong semi-diurnal tidal current may for example enhance the bottom friction for a weaker diurnal tidal constituent. Hence, in order to model the bottom friction for the diurnal tide the semi-diurnal current should be included in eq. (2.13). Alternatively one may for the diurnal tide use a linear bottom friction and increase the value of the friction coefficient in order to allow for the interaction with a strong semi-diurnal component. A linear bottom friction law may be modelled by choosing

$$k = c_f u_s,$$

where u_s is a typical velocity scale for the tidal currents.

Although the bottom friction is the dominant damping mechanism for the simulations reported here we have also investigated the effect of the lateral friction. This is modelled by

$$B_x = \nu m^2 \nabla^2 U, \tag{2.14}$$

$$B_y = \nu m^2 \nabla^2 V, \tag{2.15}$$

where ν is the horizontal eddy viscosity and the Laplace operator $\nabla^2 = \partial^2/\partial x^2 + \partial^2/\partial y^2$. The eddy viscosity is related to water depth in a similar way as proposed by Schwiderski (1980a)

$$\nu = qh, \tag{2.16}$$

where q is a constant which typically is chosen as $100\ \mathrm{m\ s^{-1}}$. This leads to an eddy viscosity between $10^3\ \mathrm{m^2\ s^{-1}}$ and $3 \cdot 10^5\ \mathrm{m^2\ s^{-1}}$ when h varies between 10 m and 3000 m.

The astronomic tide-generating potential is conveniently decomposed in a series (Schwiderski, 1980a). The components of the force; $\partial\bar{\eta}/\partial x$ and $\partial\bar{\eta}/\partial y$ are evaluated for the semi-diurnal and the diurnal equilibrium tide and analytical expressions are given in the Appendix.

The equation for the tidal energy is deduced from (2.6) and (2.7) and may when $B_x = B_y = 0$ and $\bar{\eta}$ is negligible be written

$$\frac{\partial}{\partial t}\left(\frac{U^2 + V^2 + gh\eta^2}{2hm^2}\right) = -g\nabla\cdot\left(\frac{\eta \boldsymbol{U}}{m}\right) - \frac{C_f}{m^2 h^3}(U^2 + V^2)^{\frac{3}{2}},$$

where $\boldsymbol{U} = (U, V)$ is the volume flux vector and $\nabla\cdot$ is the 2-D divergence operator. The left-hand side represents the rate of change of the kinetic and potential energy (per unit mass). The first term on the right-hand side is the net energy flux and the second term is the dissipation of energy with a quadratic bottom friction.

The energy flux F_n through a section Γ can be evaluated by the line integral

$$F_n = \rho g \int_\Gamma \frac{\eta U_n}{m}\, ds \tag{2.17}$$

where U_n is the flux component normal to the line section, ds denotes the line element and ρ is the density of sea water.

3. Boundary conditions

The boundary of the model basin consists of the coastal boundary sections Γ_c and the open boundary sections Γ_o where the basin is connected to the North Atlantic and adjacent seas through narrow passages (Fig. 1). The natural boundary conditions along the coastal boundaries are zero volume flux normal to the boundary, i.e.,

$$U_n = 0 \quad \text{along} \quad \Gamma_c. \tag{3.1}$$

Along the open boundary, one may specify the surface elevation

$$\eta = H_o \cos(\omega t - G_o) \quad \text{along} \quad \Gamma_o, \tag{3.2}$$

where $H_o = H_o(\Gamma_o)$ is the amplitude and $G_o(\Gamma_o)$ is the phase of the tidal constituent with angular velocity ω. The phase lag G_o is relative to the generating potential on the Greenwich Meridian and time (t) is GMT. It is also possible to specify the corresponding volume flux normal to the boundary

$$U_n = U_{no} \cos(\omega t - \delta_o) \quad \text{along} \quad \Gamma_o \tag{3.3}$$

where $U_{no} = U_{no}(\Gamma_o)$ is the amplitude and $\delta_o = \delta_o(\Gamma_o)$ is the phase. If H_o, G_o, U_{no} and δ_o are obtained by interpolation of empirical data or data generated by other models the two sets of boundary conditions, (3.2) and (3.3) may not be fully consistent and therefore lead to different results for the co-oscillating tide within the model basin. It should also be noted that the forced motion corresponding to the boundary conditions (3.2) and (3.3) are associated with different sets of transient free eigen-oscillations with boundary conditions

$$\eta = 0 \quad \text{along} \quad \Gamma_o,$$

and

$$U_n = 0 \quad \text{along} \quad \Gamma_o,$$

respectively. Numerical simulation with the boundary conditions (3.2) and (3.3) may also for this reason lead to different results for the amplitude and phase of the co-oscillating tide. This will in particular be important when the frequency of the eigen-oscillation is close to the frequency of the forced motion at the boundary. Since the boundary conditions (3.2) and (3.3) correspond to different sets of eigen-oscillation one may be close to resonance condition in one case and far from resonance in another. The implication for numerical simulation of the tide in the Norwegian Sea has been discussed by Gjevik and Brembo (1984).

We have also applied a third type of boundary condition where both η and U_n are specified but with adjustments imposed by a radiation condition similar to the condition used with success by Flather (1976). With the volume flux specified according to (3.3) an estimate of the surface displacement (η') can be computed along Γ_o from the continuity equation (2.8). A modified value for the volume flux is subsequently determined by a radiation condition

$$U_n' = U_n + \sqrt{gh}(\eta' - \eta), \tag{3.4}$$

where U_n and η are the specified input. It may be added that a radiation condition of the form (3.4) would be strictly correct for Sverdrup or Kelvin waves impinging normally on the boundary in a basin of uniform depth.

For the numerical simulations reported below the boundary values for H_o, G_o, U_{no} and δ_o are obtained by interpolating model data from the northeast Atlantic model by Flather (1981) and Flather et al. (1987) and data from Schwiderski's (1979, 1981 and 1986) tidal charts.

Further details of the implementation of the boundary conditions are given in Section 4.

4. Numerical method

The equations (2.6)–(2.8) are approximated by a set of finite-difference equations. We have used the staggered "Arakawa C-grid" (Mesinger and Arakawa, 1976) where the volume flux (U, V) and the surface displacement (η) are evaluated in separate points with a grid size $\Delta x = \Delta y = 2\Delta s = 50$ km (see Fig. 3). The surface displacement (η) and the volume flux (U, V) are also staggered in time. For the time integration we have used centered differences except for the Coriolis terms which are represented in an alternating way and the friction terms which are represented in a forward manner. The Coriolis terms are also represented by a four-point space average. We write $x = \Delta x i$, $y = \Delta y j$ and $t = \Delta t n$ where i, j and n are integers and the resulting difference equations read

$$\eta_{ij}^{n+1} = \eta_{ij}^n - \gamma m_{ij}^2 [\delta_x(U_{ij}^n/m_{ij}) + \delta_y(V_{ij}^n/m_{ij})], \tag{4.1}$$

$$U_{\alpha j}^{n+1} = U_{\alpha j}^n + f\Delta t\, \bar{V}_{\alpha j}^n - m_{\alpha j} g h_{\alpha j} \gamma \delta_x(\eta_{\alpha j}^{n+1} - \tilde{\eta}_{\alpha j}^{n+1}) + (A_x^n + B_x^n)\Delta t, \tag{4.2}$$

$$V_{i\beta}^{n+1} = V_{i\beta}^n - f\Delta t\, \bar{U}_{i\beta}^{n+1} - m_{i\beta} g h_{i\beta} \gamma \delta_y(\eta_{i\beta}^{n+1} - \tilde{\eta}_{i\beta}^{n+1}) + (A_y^n + B_y^n)\Delta t, \tag{4.3}$$

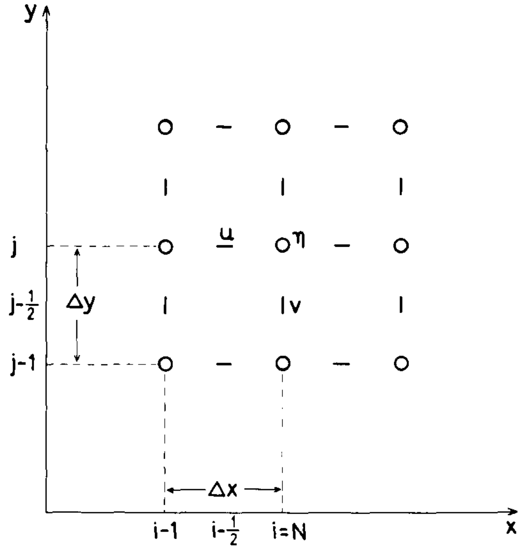

Fig. 3. Arrangement of staggered space grid with surface elevation grid point (O) and volume flux grid point (—) (|).

where the i, j and n indices denote the time and space discretization respectively $\alpha = i - \frac{1}{2}$, $\beta = j - \frac{1}{2}$, and $\gamma = \Delta t / 2\Delta s$. The difference- and averaging-operators are defined by

$$\delta_x \phi_{qj} = \phi_{q+\frac{1}{2},j} - \phi_{q-\frac{1}{2},j},$$

$$\delta_y \phi_{ip} = \phi_{i,p+\frac{1}{2}} - \phi_{i,p-\frac{1}{2}},$$

$$\overline{\phi}_{pq} = \tfrac{1}{4}[\phi_{p+\frac{1}{2},q+\frac{1}{2}} + \phi_{p+\frac{1}{2},q-\frac{1}{2}} + \phi_{p-\frac{1}{2},q-\frac{1}{2}} + \phi_{p-\frac{1}{2},q+\frac{1}{2}}].$$

The depth matrix is read from bathymetric charts for the (i, j) grid points and the depth at the intermediate points (α, j) and (i, β) are obtained by linear interpolation. As finite difference representation of the quadratic bottom friction law, we have used

$$A_x^n = -c_f[(U_{\alpha j}^n)^2 + (\overline{V}_{\alpha j}^n)^2]^{\frac{1}{2}}\, U_{\alpha j}^n / h_{\alpha j}^2,$$

$$A_y^n = -c_f[(\overline{U}_{i\beta}^{n+1})^2 + (V_{i\beta}^n)^2]^{\frac{1}{2}}\, V_{i\beta}^n / h_{i\beta}^2.$$

With the linear friction, the same expressions are applied provided the square root is replaced with a constant scaling velocity (u_s). Finally the lateral friction terms (2.14) and (2.15) are represented by a standard centered difference and applied only in the interior of the basin.

A discussion of the stability and dispersion properties of the numerical scheme for the case $\tilde{\eta} = 0$, $(A_x, A_y) = 0$, $(B_x, B_y) = 0$, m = constant and h = constant are given by Martinsen et al. (1979). In this case the scheme is neutrally stable when

$$\Delta t \leqslant \Delta s \left(\frac{2}{gmh}\right)^{\frac{1}{2}}.$$

The scheme is found to perform well with varying depth by using $mh = (mh)_{max}$ in the stability condition above. With $\Delta s = 25$ km and a maximum water depth of 4000 m the time step has to be chosen less than 173 s. It should be noted that although the spatial differentiating is correct to second order the time differentiating is only of first order due to the special time stepping used for the Coriolis terms.

The boundary conditions at the open boundary are implemented in the following way: consider for example that the boundary is a straight line located at the grid points $i = N$ (see Fig. 3).

If the surface elevation ($\eta_{i=N,j}$) is specified (eq. (3.2)), the four-point averaging of the Coriolis terms in eq. (4.3) has to be modified at the boundary and we have to use a two-point average over interior field values.

If the component of the volume flux normal to the boundary ($U_{i=N-\frac{1}{2},j}$) is specified (eq. (3.3)) no modification of the scheme is required and the interior field can be computed directly from the difference equations (4.1)–(4.3).

For the third version (eq. (3.4)) of the open boundary condition we applied the continuity equation (4.1) with $U_{i=N-\frac{1}{2},j}$ specified and obtained an estimate of the surface displacement $\eta_{i=N,j}$. A modified value of the volume flux normal to the boundary is subsequently computed from eq. (3.4) and the momentum equations (4.2) and (4.3) are finally used with the modified volume flux to compute the interior field.

5. The M_2 tide

M_2 simulations have been carried out with different versions of the model in order to assess the effects of open boundary conditions, tide generating forces, horizontal eddy viscosity, etc. We have considered five model modifications:

I: volume flux and surface elevation prescribed at open boundaries with adjustments imposed by the radiation condition eq. (3.4). Tide generating force with correction for elastic yielding, quadratic bottom friction and horizontal eddy viscosity are included.

II: same as I but without eddy viscosity.

III: same as I but without tide generating force.

IV: volume flux prescribed at open boundary (eq. (3.3)). Otherwise as I.

V: surface elevation prescribed at open boundary (eq. (3.2)). Otherwise as I.

Input data for volume fluxes and surface elevation along the open boundary sections A–B–C, D and E (Fig. 1) are obtained from the northeast Atlantic model by Flather (1981) and from the tidal charts by Schwiderski (1979). The model parameters used for the simulations are:

Grid size	$2\Delta s$	$= 50$ km
Time step	Δt	$= 168.3$ s
Bottom friction coefficient	c_f	$= 0.003$
Eddy viscosity coefficient	q	$= 100$ m s^{-1}

The simulations are started from rest and a steady state of oscillations is normally approached after 2–4 cycles. This is illustrated by Fig. 4 which shows time series of the surface elevation at two island stations; Jan Mayen in the Norwegian Sea and Bear Island in the Barents Sea.

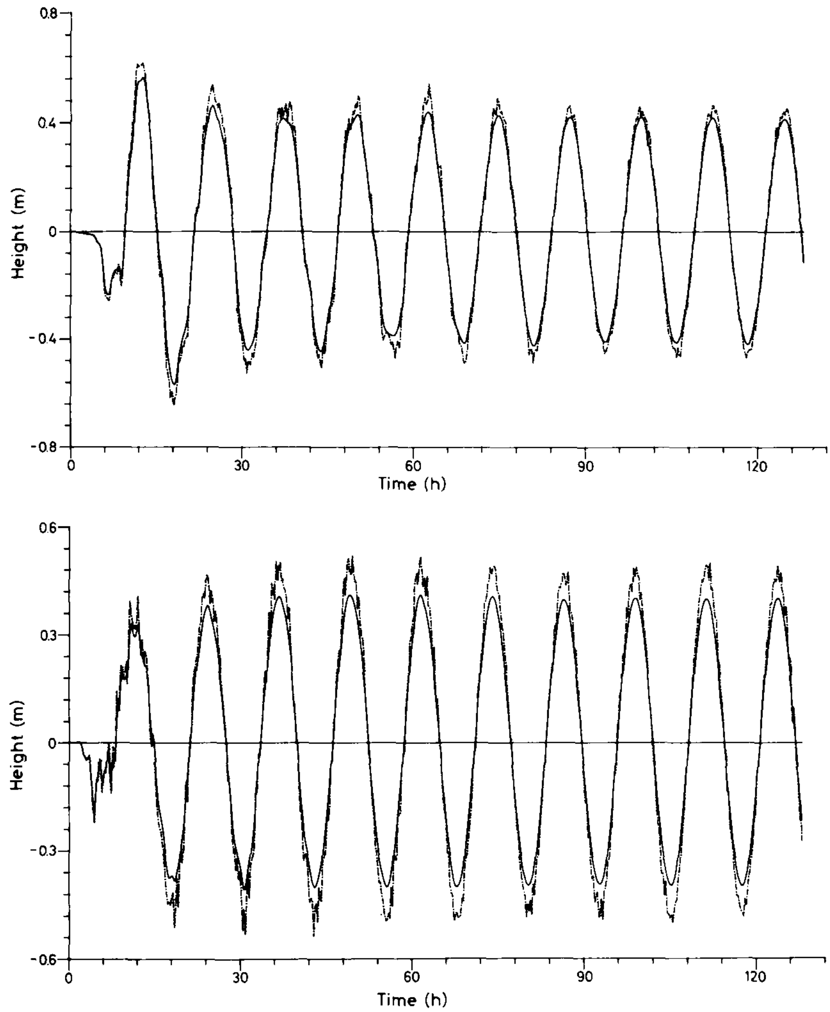

Fig. 4. Time series of M_2 surface elevation for two island stations, Jan Mayen in the Norwegian Sea (lower panel) and Bear Island in the Barents Sea (upper panel). Full drawn line model I. Broken line model II.

To ensure that a steady state is reached, the simulations are run for 120 h and harmonic constants for the surface elevation; amplitude (H) and phase (G) relative Greenwich are determined during the following cycle. The corresponding tidal current is described by the parameters of the tidal ellipse; major half-axis (A) minor half-axis (B), azimuth angle of the major axis (θ), the Greenwich phase lag of the current vector and the direction of rotation. By interpolation, the harmonic constants are determined at stations where comparison with observations can be made. A selection of 116 tidal stations mostly in the Nordic Seas (Fig. 2), but also including a few stations in the Arctic Ocean, have been used for comparing harmonic constants for surface elevation. Current data has been compared with measurements only for a few offshore stations mainly along the Norwegian coast and in the Barents Sea.

In order to demonstrate the effects of boundary conditions, tide generating force and horizontal eddy viscosity the computed and observed harmonic constants for 15 coastal and pelagic stations are listed in Table 1. The last 6 stations on the list are pelagic stations; two with IAPSO reference, the rest are offshore oil fields. By comparing the results of model I and III we see that the tide generating force only has a minor effect on the amplitude and phase and for most stations the corrections due to the tide generating force are less than 2 cm and 5°, respectively. The horizontal eddy viscosity has a larger effect on the results and the tidal amplitudes obtained with

Table 1. *M_2 amplitude and phase*

Stations		Observed	Model I	II	III	IV	V
1. Pukhovy Bay	H (m)	0.32	0.31	0.36	0.30	0.31	0.33
72°39′N, 52°42′E	G (deg)	159	179	196	177	174	171
2. Bear Island	H (m)	0.34	0.37	0.39	0.36	0.37	0.37
74°29′N, 19°12′E	G (deg)	013	355	020	357	347	354
3. Hammerfest	H (m)	0.88	0.83	0.98	0.84	0.81	0.86
70°40′N, 23°41′E	G (deg)	020	021	017	024	011	021
4. Rørvik	H (m)	0.78	0.77	0.84	0.75	0.73	0.79
64°52′N, 11°15′E	G (deg)	313	315	307	315	312	312
5. Stavanger	H (m)	0.15	0.20	0.23	0.20	0.19	0.20
58°59′N, 5°44′E	G (deg)	270	309	289	304	304	303
6. North Shields	H (m)	1.58	1.73	1.94	1.69	1.64	1.75
55°01′N, 1°26′W	G (deg)	089	126	134	123	116	122
7. Scolpaig Bay	H (m)	1.19	1.16	1.14	1.18	1.20	1.18
57°39′N, 7°30′W	G (deg)	177	190	190	189	175	188
8. Djubvogur	H (m)	0.65	0.54	0.63	0.51	0.61	0.56
64°40′N, 14°17′W	G (deg)	097	100	086	101	090	103
9. Jan Mayen	H (m)	0.41	0.40	0.49	0.40	0.41	0.41
10°58′N, 8°41′W	G (deg)	344	349	344	348	341	346
10. Reykjanes Ridge	H (m)	0.91	0.82	0.86	0.80	0.73	0.90
62°50′N, 24°43′W	G (deg)	180	189	185	189	179	189
11. Shetland Region	H (m)	0.44	0.48	0.55	0.47	0.44	0.50
63°08′N, 0°00′W	G (deg)	288	300	302	298	294	300
12. Statfjord	H (m)	0.51	0.55	0.62	0.55	0.51	0.57
61°15′N, 1°51′E	G (deg)	286	308	320	305	299	304
13. Frigg	H (m)	0.42	0.46	0.52	0.46	0.44	0.48
59°53′N, 2°04′E	G (deg)	297	330	339	328	323	330
14. Ekofisk	H (m)	0.28	0.20	0.25	0.20	0.19	0.21
56°33′N, 3°13′E	G (deg)	078	110	123	107	100	103
15. Shelf west of Norway	H (m)	0.63	0.62	0.72	0.61	0.61	0.64
66°55′N, 8°08′E	G (deg)	324	330	328	327	319	325

the model with zero eddy viscosity (model II) are 5–25% higher than the corresponding values computed with model I. The time series displayed in Fig. 4 which corresponds to model I and II also demonstrates the smoothing effect which the horizontal eddy viscosity has on short period noise. The results of the simulations with different open boundary conditions (models I, IV and V) show that different boundary conditions lead to variation in the computed amplitudes of the order 5–15%. The differences are generally largest closest to the open boundary and in particular in the regions around Iceland and Scotland. The results for stations in the northern part of the model area; the Barents Sea and the Arctic Ocean is less affected. The performance of the model simulations with different boundary conditions is illustrated by the correlation coefficients between computed and observed data (amplitude/phase) which are given for groups of stations in Table 2.

These results show that the best overall performance is obtained with model IV. This model also shows a significantly better agreement with observation for stations along the coast of Great Britain and Ireland than the models I and V. The scatter diagrams for the comparison between computed and observed amplitude and phase for model IV are shown in Fig. 5. The linear regression line for the amplitude data has a coefficient 0.90 and intercept +0.04 m on the axis for computed values and a standard deviation ±0.11 m. The corresponding values for the phase data are 0.89, +26.6° and ±33.4°. The few very scattered points all belong mostly to stations along the coast of Great Britain and Ireland and the finer details of the tide in this region are obviously not resolved well with a grid size of 50 km. The performance of the model is particularly good in the Barents Sea and along the northern and western coast of Norway. For this region model V is the best with standard deviations ±0.09 m and ±43° for the linear regression between computed and measured values. The eastern part of the North Sea including Skagerrak and Kattegat are areas with relatively

Table 2. *Correlation coefficients between computed and observed M_2 constants (amplitude/phase)*

Stations	Model I	Model IV	Model V
All 116 stations	0.92/0.94	0.97/0.95	0.93/0.94
Barents Sea and Norwegian coast (24 stations)	0.98/0.92	0.98/0.92	0.98/0.92
Pelagic (27 stations)	0.95/0.97	0.94/0.97	0.94/0.97
Coast of Great Britain (23 stations)	0.49/0.94	0.92/0.99	0.54/0.96

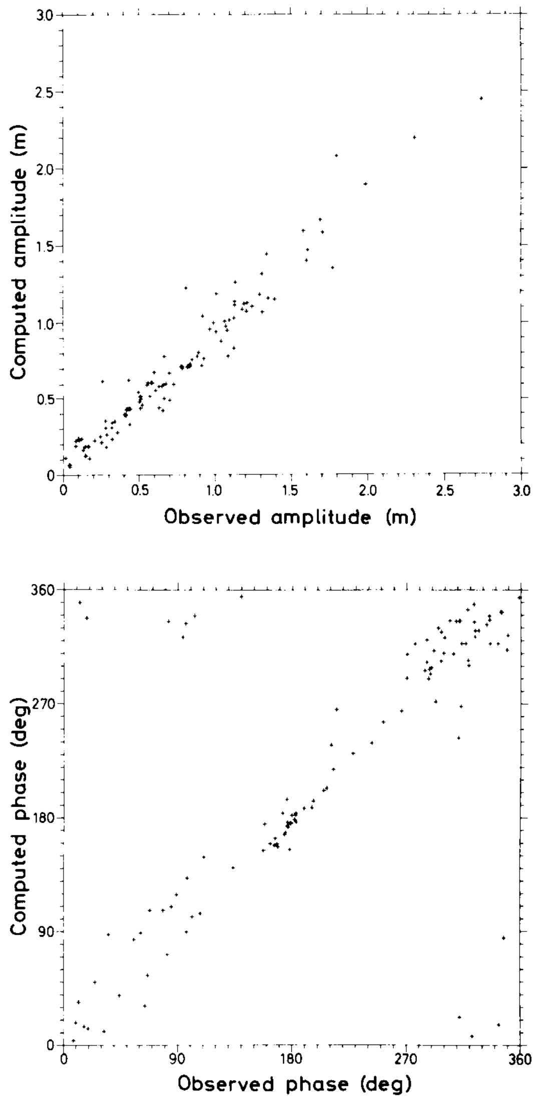

Fig. 5. Scatteirng diagrams for comparison between observed and computed M_2-amplitude (upper graphs) and phase (lower graphs). Model IV.

large differences between computed and observed values both for amplitude and phase. This may be due to a coarse grid representation of the Norwegian Trench and an insufficient model for the flow through the Strait of Dover. The neglect of the tidal interaction with the Baltic Sea through Kattegat may also have some effect.

Co-range and co-tidal lines obtained with model IV for the Norwegian and Barents Seas with adjacent waters are displayed respectively in Figs. 6 and 7. These maps show main amphidromes in strait between Iceland and Greenland, on the Iceland–Faeroe Rise and in the eastern part of the North Sea. This agrees well with the results by Flather (1981), Cartwright et al. (1980).

Distortions of the co-tidal and co-range lines in the vicinity of the Faeroes and Shetland–Orkney islands are clearly revealed by the model. Since these islands are too small to be represented as land points ($h = 0$) by the grid, the effect of the islands is introduced by requiring zero volume flux.

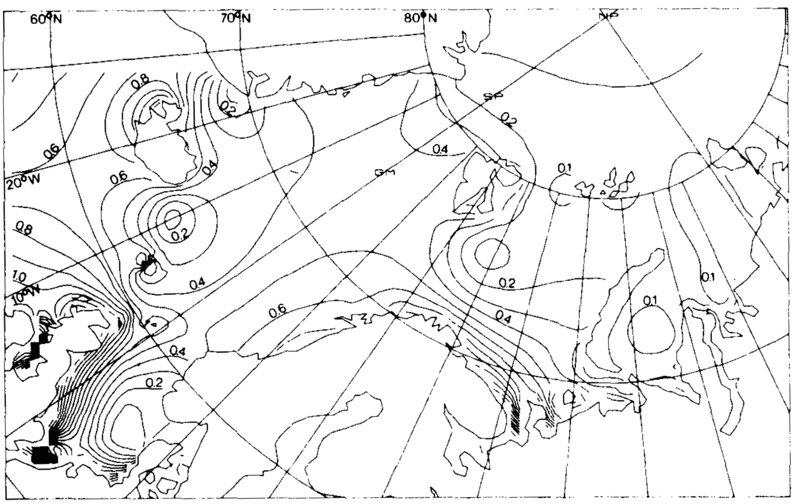

Fig. 6. Co-range lines for the M_2 tide in the Nordic Seas. Model. IV. Equidistance 0.1 m.

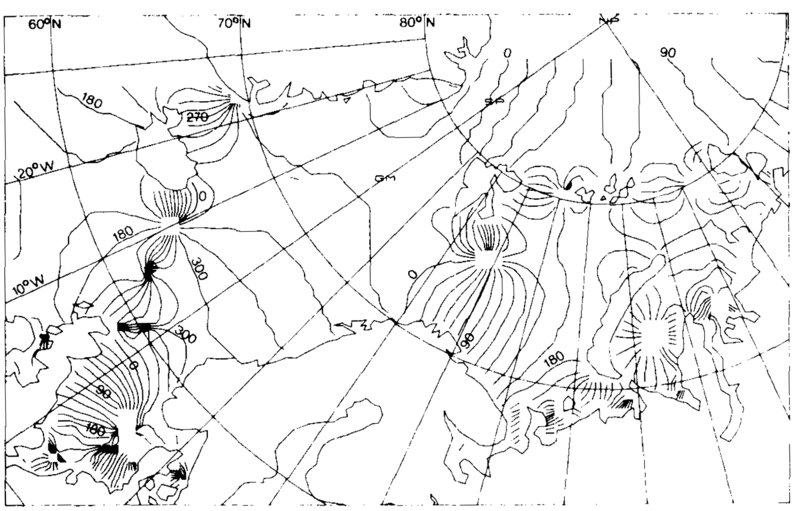

Fig. 7. Co-tidal lines for the M_2 tide in the Nordic Seas. Model IV. Equidistance 15°.

The model also reveals a main amphidrome in the Barents Sea north-east of Bear Island. The existence of this amphidrome has been a matter of some dispute. It was clearly resolved by the charts constructed by Nekrasov (1961) mainly on basis of observational data. New data (see Gjevik, 1988) do also support the existence of an amphidrome. The recent charts by Schwiderski (1986) do, however, show only an incomplete amphidrome in this region.

The principal axis of the current ellipse and the direction of rotation of the current vector are shown for the Norwegian and the Barents Seas and adjacent waters in Figs. 8 and 9. These results as well as those in Table 3 are obtained with model IV.

Most of the stations listed in Table 3 are located in areas on the Norwegian continental shelf where major offshore oil production facilities already have been built or are being

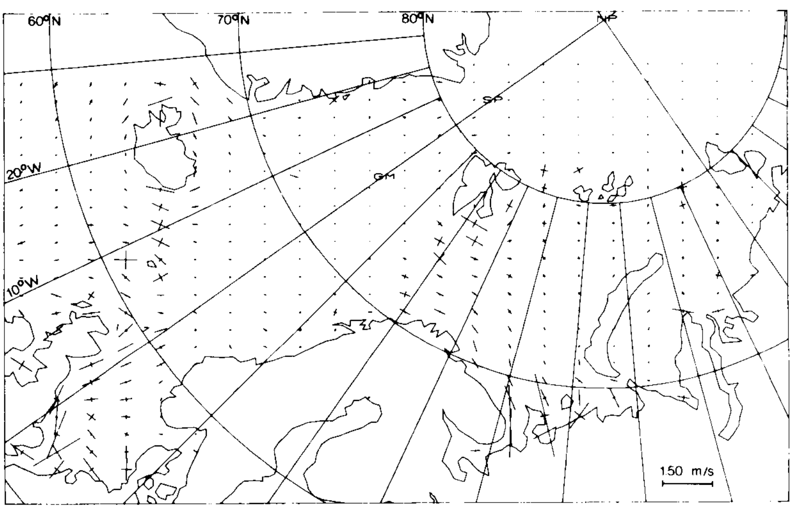

Fig. 8. Principal axis of M_2 current ellipse in the Nordic Seas. Model IV.

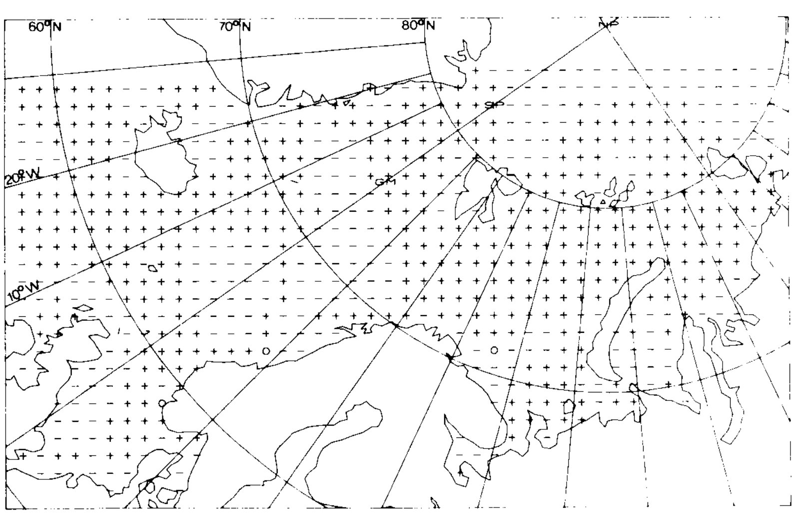

Fig. 9. Sense of rotation of the M_2 current vector in the Nordic Seas. + clockwise, − counter-clockwise. Model IV.

Table 3. *Computed parameters for the M_2 current ellipse (model IV)*

Station	Major half-axis A cm s^{-1}	Minor half-axis B cm s^{-1}	Azimuth angle of A degree	Rotation (+ clockwise)
Statfjord (61°15′N, 1°51′E)	11.5	4.9	171	+
Haltenbanken (65°03′N, 7°35′E)	5.7	0.7	074	+
Trænabanken (66°18′N, 9°31′E)	3.0	2.8	062	−
Shelf Edge (66°55′N, 8°08′E)	2.9	1.5	013	−
Tromsøflaket (71°30′N, 19°00′E)	16.0	7.7	077	+
South of Bear Island (74°00′N, 20°00′E)	21.2	13.0	096	+
Sentralbanken (74°31′N, 31°06′E)	9.4	2.2	096	+
Fram Strait (80°00′N, 0°00′E)	3.6	0.2	179	+

Table 4. *M_2 energy flux (Gigawatt)*

Section	Model I	Model IV	Model V
Greenland–Iceland (northward)	28.4	40.3	24.1
Iceland–Faeroes (northward)	25.9	10.8	28.0
Faeroes–Scotland (northward)	75.5	62.4	76.3
Scotland–Norway (southward)	28.9	24.3	30.4
Dover Strait (northward)	15.6	7.7	10.8
Northern Norway–Spitsbergen (eastward)	39.4	35.3	41.4
Fram Strait (northward)	26.5	23.6	27.1
Spitsbergen–Franz Josef Land (northward)	5.1	4.8	5.4
Franz Josef Land–Severnaya Zemlya (northward)	4.5	4.0	4.6

planned. Prediction of tidal currents are therefore important for establishing reliable design criteria. A detailed comparison between the current predictions and observational data is given by Gjevik (1988) and for most of the stations in Table 3 the agreement is found to be very good.

We note the intensification of the currents in the Barents Sea particularly in the region between Bear Island and Spitsbergen, in the western part of the North Sea and on the Iceland–Faeroes Rise. This picture is generally in good agreement with observations but so far we have made no attempt at undertaking a systematic comparison for a large number of stations. The geographical variation of the direction of rotation (Fig. 9) shows an interesting pattern distribution. For the North Sea main features of this pattern compare well with the spatial distribution of the sense of rotation obtained by other model simulations (Davies, 1986). It may also be noted that the observed change in sense of rotation on the shelf west of Norway is reproduced well by the model simulations for Haltenbanken and Trænabanken (Table 3). Current measurements along a line from northern Norway to Bear Island (Huthnance, 1981) show clockwise rotation of the M_2 current and the observed current speed and rotation agree well with the computed results. The computed parameters of the current ellipse for two stations along this line; Tromsøflaket and Bear Island; are listed in Table 3.

Energy fluxes are computed for some key sections of the model basin and results for model I, IV and V are shown in Table 4. We note that the flux-driven model (IV) strongly affects the energy flux in the region around Iceland as compared to the results for models I and V. The total energy flux through the sections Greenland–Iceland–Faeroes Islands is however nearly the same for all three models. This is also true for the other section except the Dover Strait. Based on these results we obtain the energy budget (mean values) for the M_2 tide shown in Table 5.

If we allow for energy dissipation west of Scotland the calculated mean energy flux for model I, IV and V into the Norwegian Sea through a section from Scotland over Faeroes to Iceland of 93.6 Gw is reasonably consistent with Cartwright et al.'s (1980) estimated flux of 120 Gw between Eire and Iceland. Also the calculated mean energy flux for the same three models from the Norwegian–Greenland Seas into the Barents Sea and the Arctic Ocean of about 64 Gw agrees well with Kowalik and Untersteiner's

Table 5. *M_2 energy budget*

Energy flux into Norwegian–Greenland Seas from the North Atlantic	124 Gw
Energy dissipation in Norwegian–Greenland Seas	32 Gw
Energy dissipation in the North Sea	39 Gw
Energy flux into the Barents Sea from the Norwegian–Greenland Seas	39 Gw
Energy dissipation in the Barents Sea	34 Gw
Energy flux into the Arctic Ocean from the Greenland–Norwegian–Barents Seas	35 Gw

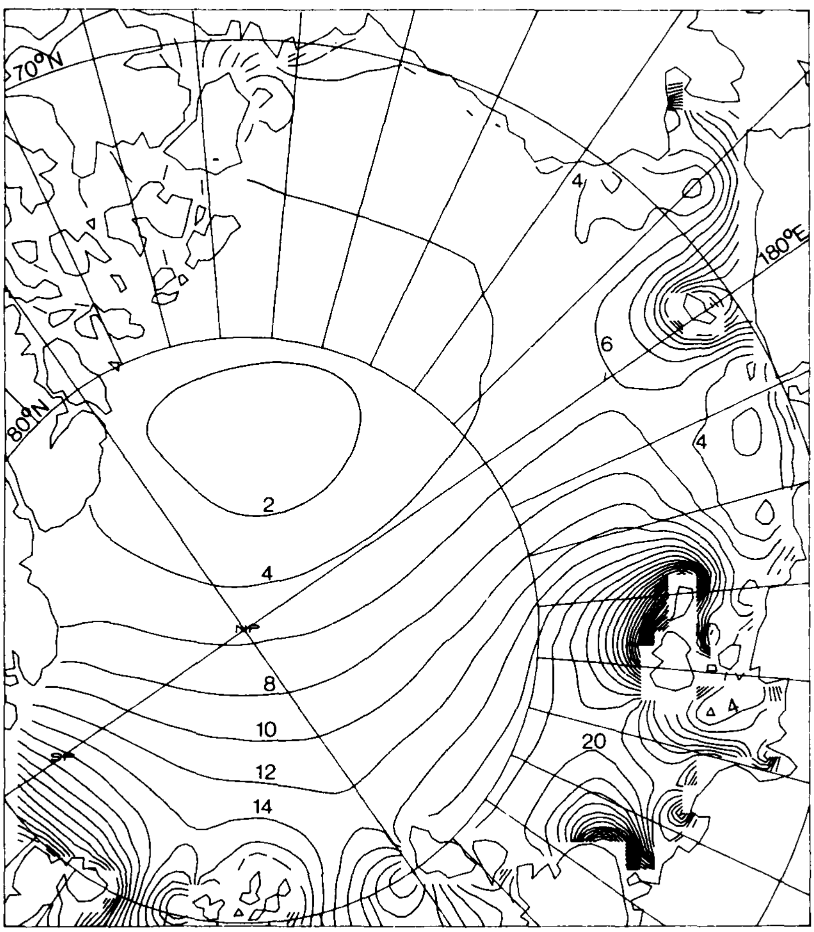

Fig. 10. Co-range lines for the M_2 tide in the Arctic Ocean. Model IV. Equidistance 2 cm.

(1978) estimated 70 Gw energy dissipation in the Arctic and the Barents Sea. The mean value for the energy flux obtained with model I, IV and V for a section from Scotland to Norway is 27.9 Gw which compares well with Flather's (1976) estimate of 35.6 Gw for nearly the same section if we allow for the fact that Flather's estimate also includes the S_2 flux. The relatively large differences in energy flux values between model IV and V particularly for sections near the open boundary indicate that the energy flux calculation is sensitive to boundary conditions of the model. The results obtained with model V probably provide the best estimates.

Computed tidal charts for the Arctic Ocean based on model IV are shown on Figs. 10 and 11. A main amphidrome in the Arctic Ocean is found with center at (83° N, 270° W) which is in good agreement with earlier results by Kowalik and Untersteiner (1978) and Schwiderski (1979). Maps showing current ellipse and the direction of rotation of the current vector corresponding to the charts in Figs. 10 and 11 are given by Gjevik and Straume (1986). It is interesting to see that the primarily clockwise rotation of the current vector on the broad Euroasian shelf is supported by the early current measurements by Sverdrup (1926).

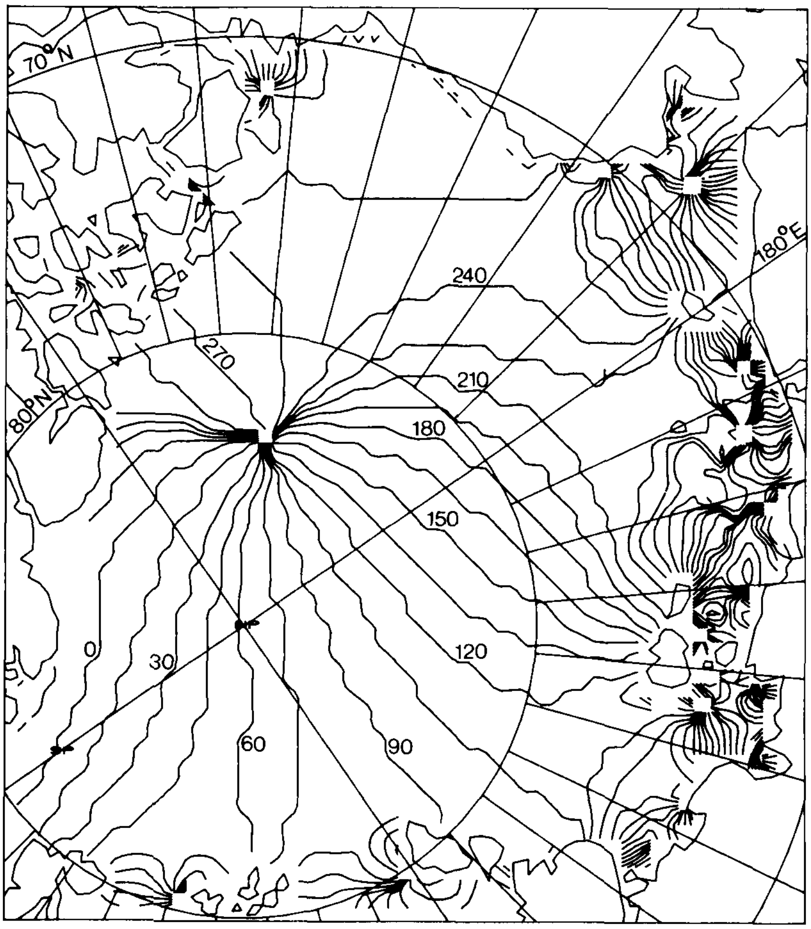

Fig. 11. Co-tidal lines for the M_2 tide in the Arctic Ocean. Model. IV. Equidistance 15°.

6. The K_1 tide

K_1 simulations have also been carried out with different versions of the model in order to assess the sensitivity of the results to changes in boundary conditions, the effect of tide generating forces, and eddy viscosity. A similar set of model modifications as listed I–IV in Section 5 have been tested, but instead of a quadratic bottom friction we have for the diurnal tide applied a linear friction law with an increased friction coefficient as explained in Section 2. A constant velocity scale with $u_s = 0.75$ m s^{-1} has been used in most simulations. The effect of a spatial current variation has been tested by using the maximum M_2 current as velocity scale. This leads to an increase of K_1 amplitude up to 20% for some stations. The large scale features of the variation of amplitude and phase within the model basin are however unchanged.

The input data for volume fluxes and surface elevation along the open boundary sections A–B–C, D and E (Fig. 1) are also for the K_1 simulations based on results obtained with the north-east Atlantic model by Flather (1981) and on tidal charts by Schwiderski (1981). The model parameters; grid size, time step and eddy viscosity coefficient have the same values as used for the M_2 simulations.

A steady state of oscillation is normally approached after 3–4 cycles. The total simulation time is, however, extended to 240 h in order to ensure that a steady state is reached before the harmonic constants for the surface elevation and the parameters for the current ellipse are evaluated. Comparison with observed harmonic con-

Table 6. *K_1 amplitude and phase*

Stations		Observed	Model I	II	III	IV	V
1. Pukhovy Bay	H (cm)	4.9	5.4	6.0	5.4	5.5	4.7
72°39′N, 52°42′E	G (deg)	170	352	334	314	010	349
2. Bear Island	H (cm)	5.4	6.9	7.3	7.4	6.9	6.4
74°29′N, 19°12′E	G (deg)	211	182	174	181	182	174
3. Hammerfest	H (cm)	8.1	11.1	12.8	11.7	10.9	9.9
70°40′N, 23°41′E	G (deg)	214	212	192	193	214	206
4. Rørvik	H (cm)	7.4	9.2	10.5	11.5	8.8	8.2
64°52′N, 11°15′E	G (deg)	171	181	174	171	181	173
5. Stavanger	H (cm)	1.5	2.0	2.1	2.7	2.6	1.7
58°59′N, 5°44′E	G (deg)	174	221	211	215	233	211
6. North Shields	H (cm)	11.2	14.4	16.1	23.0	13.5	12.4
55°01′N, 1°26′W	G (deg)	240	258	246	251	246	245
7. Scolpaig Bay	H (cm)	4.7	11.7	11.6	13.3	11.3	9.9
57°39′N, 7°30′W	G (deg)	086	130	125	128	126	119
8. Djubvogur	H (cm)	6.6	4.3	5.8	7.2	3.5	5.7
64°40′N, 14°17′W	G (deg)	077	120	124	200	118	116
9. Jan Mayen	H (cm)	6.0	5.4	6.9	7.1	5.6	5.6
10°58′N, 8°41′W	G (deg)	116	142	136	180	140	130
10. Reykjanes Ridge	H (cm)	12.2	11.0	11.8	7.5	10.4	11.4
62°50′N, 24°43′W	G (deg)	136	135	136	146	136	136
11. Shetland Region	H (cm)	7.5	8.2	9.4	10.9	7.7	7.6
63°08′N, 0°00′W	G (deg)	157	166	164	169	165	156
12. Statfjord	H (cm)	6.1	7.8	8.7	11.2	7.5	7.0
61°15′N, 1°51′E	G (deg)	172	181	176	180	182	170
13. Frigg	H (cm)	4.5	6.2	6.9	9.2	6.1	5.5
59°53′N, 2°04′E	G (deg)	159	194	186	192	194	183
14. Ekofisk	H (cm)	2.5	4.5	5.1	6.9	4.5	4.0
56°33′N, 3°13′E	G (deg)	273	276	267	269	246	265
15. Shelf west of Norway	H (cm)	4.5	7.4	8.2	10.1	7.2	6.6
66°55′N, 8°08′E	G (deg)	171	190	181	181	192	181

stants is made for the same 116 stations as used for verification of the M_2 simulations. The observed and computed harmonic constant for the five model versions are listed in Table 6 for a selection of 15 stations. For the station Pukhovy Bay the observed phase lag is 170° while the computed phase lag range from 314°–010° depending on the type of model. The results of the model simulations compare well with Schwiderski (1981). We therefore suspect that the phase lag (170°) published in lists of observed harmonic constant are erroneous and that a correction of nearly 180° may apply in this case.

By comparing the results of model I and III we see that the tide generating force has a substantial effect on the amplitude of the diurnal tide particularly in the North Sea region and on the shelf west of Norway. For several stations the corrections due to the tide generating force are as large as 30–50%. The horizontal eddy viscosity has a minor effect on results and the tidal amplitude obtained with zero eddy viscosity (model II) are for most stations only 5–15% higher than the corresponding values obtained with model I. The results of the simulations with different boundary conditions (models I, IV and V) show that the different boundary conditions lead to variation in the computed amplitude up to about 30%. The differences are generally largest closest to the open boundaries in particular in the regions around Iceland and Scotland and in the northern part of the North Sea. The performance of the model simulation with different boundary conditions is illustrated by the correlation coefficient between computed and observed data which are given for groups of stations in Table 7.

Table 7. *Correlation coefficients between computed and observed K_1 constants (amplitude/phase)*

Stations	Model I	Model IV	Model V
All 116 stations	0.81/0.89	0.81/0.85	0.82/0.88
Barents Sea and Norwegian coast (24 stations)	0.92/0.92	0.91/0.88	0.92/0.92
Pelagic (27 stations)	0.63/0.82	0.64/0.76	0.64/0.83
Coast of Great Britain (23 stations)	0.59/0.88	0.61/0.80	0.63/0.91

The correlation coefficients show that the three models perform about equally but with a slight preference for model V. For this model the linear regression line for amplitude data has a coefficient 0.80, intercept +0.02 m on the axis for computed values and standard deviation ±0.02 m. The corresponding values for the phase data are 0.82, +32° and ±33°. The scatter diagrams for the correlation between computed and observed amplitude and phase are shown in Fig. 12.

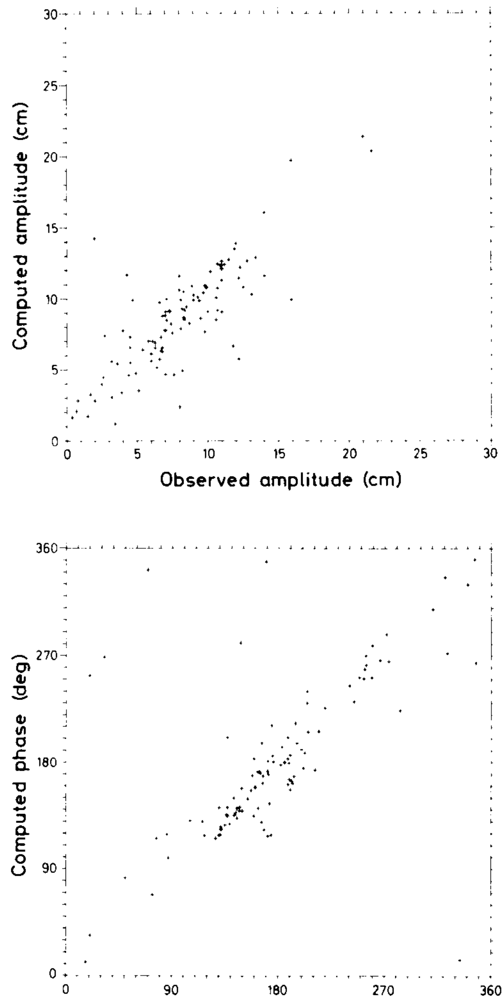

Fig. 12. Scattering diagrams for comparison between observed and computed K_1 amplitude (upper graphs) and phase (lower graphs). Model V.

Similar to what was found for M_2 we see that the model performs particularly well for stations along the northern and western coast of Norway and in the Barents Sea. Model V is best for this region with standard deviations ± 0.03 m and $\pm 35°$ for the linear regression between computed and measured values. The computed amplitudes are however, somewhat higher than the measurements with an arithmetic mean difference of about 0.01 m.

Co-range and co-tidal lines obtained with model V for the Norwegian and Barents Seas with adjacent waters are displayed respectively in Figs. 13 and 14. These maps show a main amphidrome in the Fram Strait in agreement with the results by Schwiderski (1981) and Nekrasov (1961). An amphidrome is also located in the North Sea with center in the Skagerrak. From Figs. 13 and 14 it is evident that the shelf edge between Tromsøflaket offshore northern

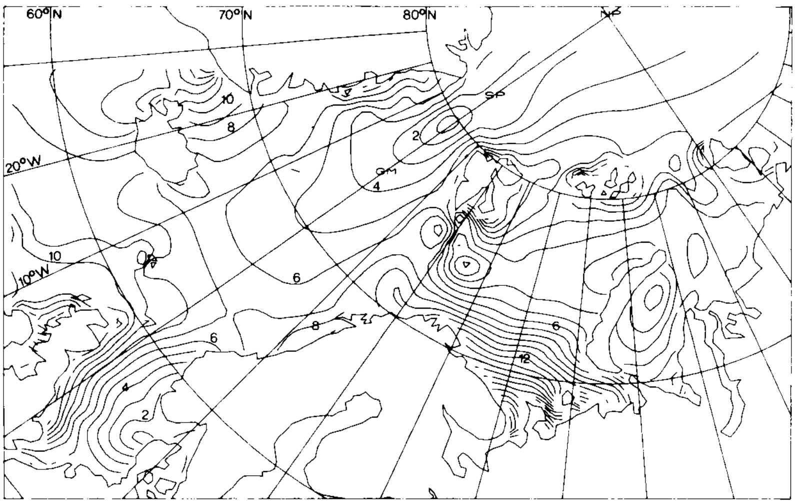

Fig. 13. Co-range lines for the K_1 tide in the Nordic Seas. Model V. Equidistance 1 cm.

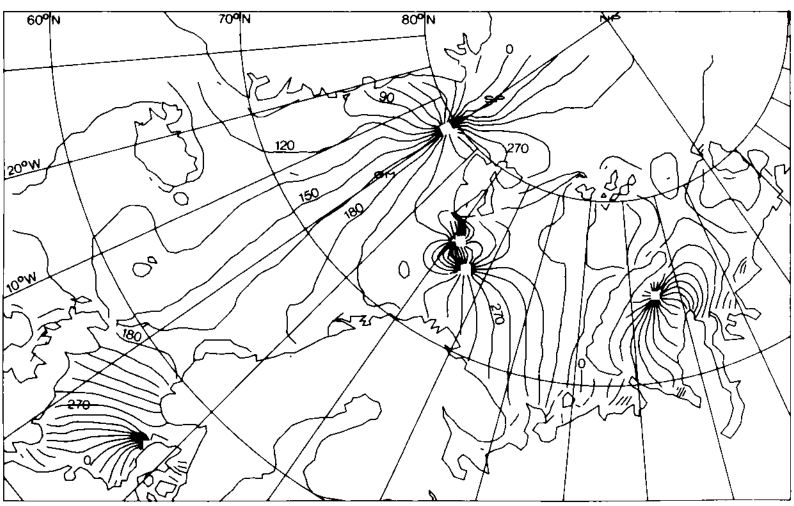

Fig. 14. Co-tidal lines for the K_1 tide in the Nordic Seas. Model V. Equidistance 15°.

Norway (71°30′N, 19°00′E) and Spitsbergen has a strong effect on the diurnal tide in this region. A well-developed amphidrome is located east of Bear Island and is connected to smaller amphidromic features in the region between Bear Island and Spitsbergen. A local maximum for K_1 amplitude is also found in the Tromsøflaket region. The small scale features may not be resolved well on a 50 × 50 km grid and it remains to be seen how a grid refinement will affect the local topographical modification of the diurnal tide in this part of the Barents Sea. Schwiderski's (1981) chart of the diurnal tide in this region is obviously an oversimplification and his K_1 tidal charts give no indication of an amphidrome in the Bear Island region.

The principal axis of the current ellipse and sense of rotation of the current vector are shown in Figs. 15 and 16, respectively. The intensification of the diurnal tidal current in Bear Island

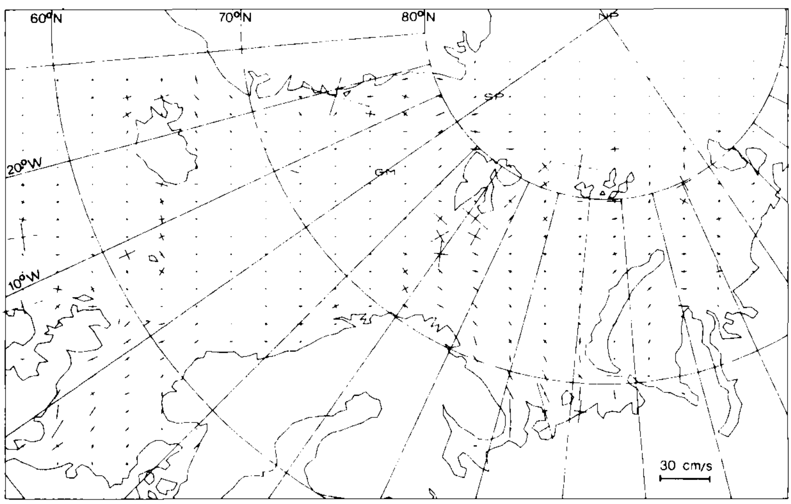

Fig. 15. Principal axis of K_1-current ellipse in the Nordic Seas. Model V.

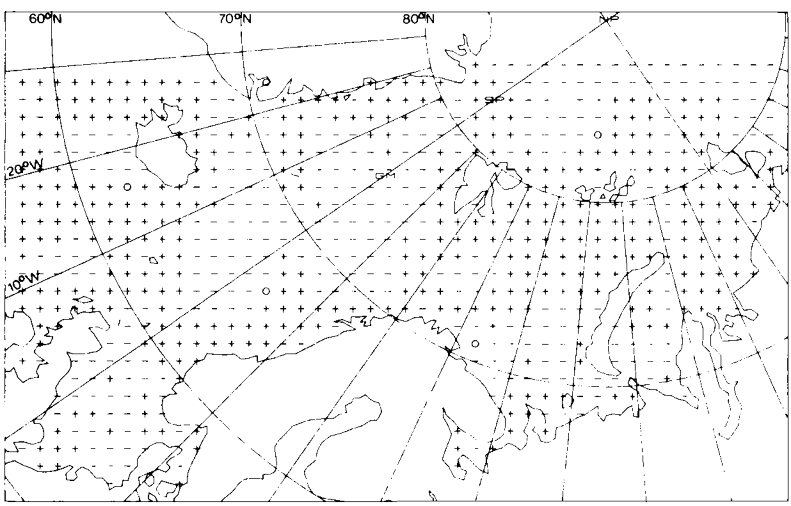

Fig. 16. Sense of rotation of M_2 current vector in the Nordic Seas. + clockwise, − counter-clockwise. Model V.

region is clearly demonstrated by Fig. 15 but the maximum current speed obtained by the model is somewhat less than the recorded extreme value of about 0.18 m/s (Huthnance, 1981). The model simulation also reveals relatively large diurnal currents on the east Greenland shelf, in the Fram Strait on the Rockall bank, the Iceland–Faeroe Rise and in the western part of the North Sea. A band shaped region with mainly clockwise current rotation stretches from the Iceland–Faeroe Rise northward along the shelf west of Norway and over to Spitsbergen along the shelf edge at the entrance to the Barents Sea. This indicates that the diurnal tide in this region has a continental shelf wave mode structure. The characteristic features are most pronounced along the section of the shelf from northern Norway to Spitsbergen and revealed clearly in regional plots of the instantaneous current field and of the mean energy flux. The model predictions agree well with current measurements from the Norwegian shelf and also the current measurement along a line from northern Norway to Spitsbergen referred by Huthnance (1981) (see Gjevik, 1988).

The energy fluxes associated with the diurnal tide are relatively small and computation for the same sections as used for computing M_2 energy fluxes (Table 4) show large variation for the three models I, IV and V. In particular, the energy flux in the Danish Strait between Iceland and Greenland is very sensitive to the type of boundary

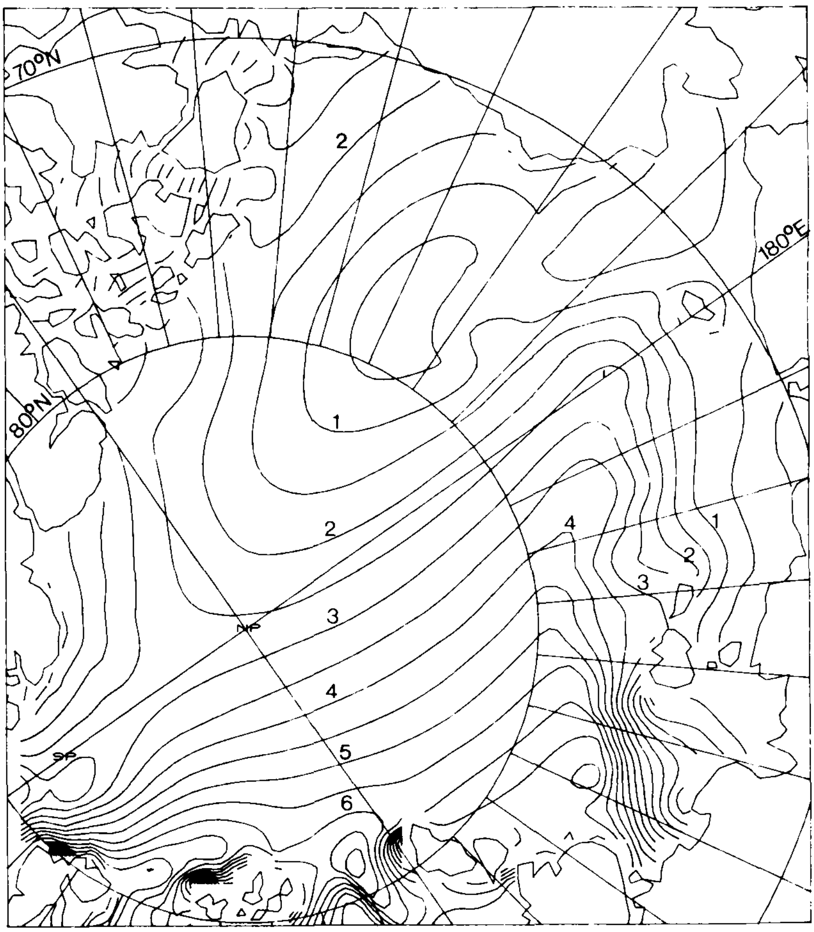

Fig. 17. Co-range lines for the K_1 tide in the Arctic Ocean. Model. V. Equidistance 0.5 cm.

condition applied at the open boundary. The total energy flux into the Norwegian–Greenland Seas from the North Atlantic Ocean is found to be from 0.8 to 2.4 Gw. The flux into the North Sea from the Norwegian Sea through the section from Scotland to Norway is 0.3–0.4 Gw and energy flux from the Norwegian Sea to the Barents Sea through the section from northern Norway to Spitsbergen is 0.8–1.0 Gw. Finally, we find a northward energy flux in the Fram Strait between 0.5 and 0.8 Gw.

K_1 tidal charts for the Arctic Ocean obtained with model V are shown in Figs. 17 and 18. A main amphidrome is found with center at (18° N, 150° W) which is in good agreement with the results obtained by Schwiderski (1981). We note that particularly in the western part of the Arctic Ocean the K_1 amplitude is relatively large compared with the M_2 amplitude and the amplitude ratio K_1/M_2 is about 0.5. Maps showing the current ellipse and the sense of rotation of the current vector can be found in Gjevik and Straume (1986).

7. Conclusions

The results obtained with the tidal model for the Norwegian–Greenland–Barents Seas and the Arctic Ocean show that the large scale features of the tide in these regions can be simulated by acceptable accuracy with a 50×50 km grid

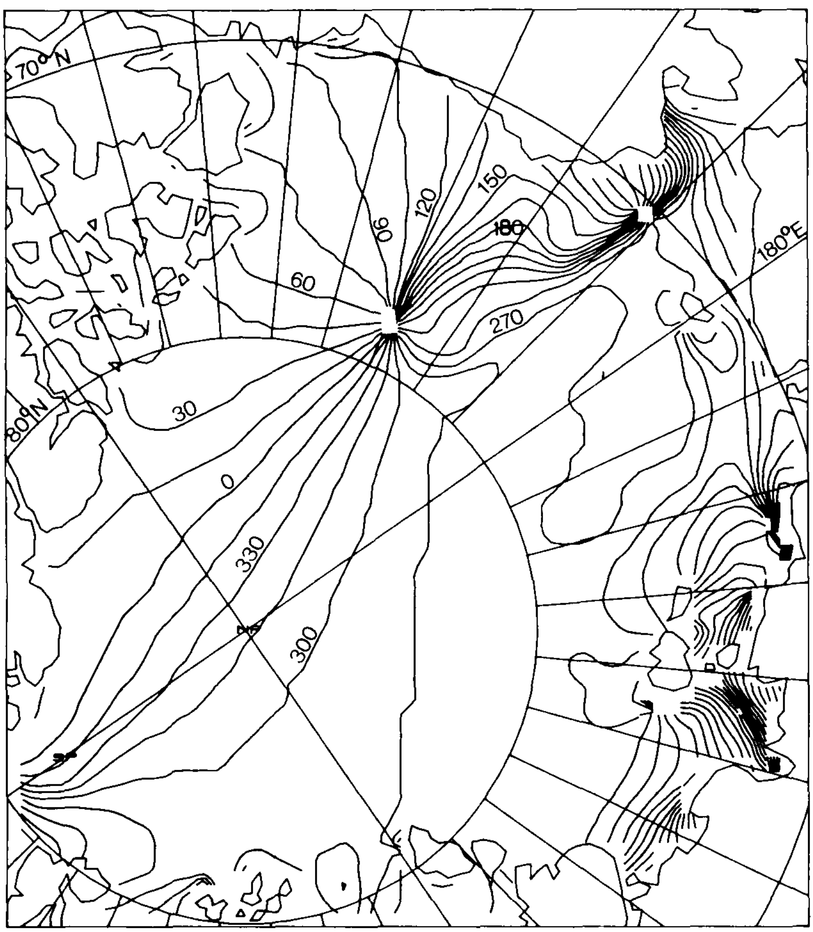

Fig. 18. Co-tidal lines for the K_1 tide in the Arctic Ocean. Model V. Equidistance 15°.

resolution. The performance of the model version V (see Sections 5 and 6) is particularly good for the continental shelf along the western and northern coast of Norway and in the Barents Sea.

The semi-diurnal M_2 tide in the Norwegian–Greenland–Barents Seas is essentially a co-oscillating tide and the effects of the direct tide generating force is small. For most stations the amplitude correction due to the tide-generating force and elastic yielding of the earth is less than 2 cm. The M_2 tide propagates into the Norwegian–Greenland Seas from the North Atlantic. The wave is partly diffracted around Scotland into the North Sea but the main part proceeds northward into the Barents Sea and the Arctic Ocean. The total energy influx from the North Atlantic is found to be about 124 Gw and of this amount about 35 Gw is transmitted into the Arctic Ocean. The rest is dissipated with a nearly equal amount in each of the three regions; the Norwegian–Greeland Seas, the Barents Sea and the North Sea.

The diurnal K_1 tide is strongly affected by the direct tide generating force. The amplitude correction due to a tide generating force and elastic yielding is in particular large in the North Sea and along the west coast of Norway. For some stations the correction is as large as 30%–50%.

The shelf edge between Vesterålen in northern Norway and Spitsbergen which forms the boundary between the shallow Barents Sea on the eastern side and the deeper Norwegian Sea on the western side has a strong effect on tidal currents and amplitudes in this region. The topographical relief leads to an enhancement of the tidal currents with a relatively large diurnal component particularly in the region near Bear Island.

The model predicts amphidromes near Bear Island both for the dominant semi-diurnal and the diurnal components. The small scale variations of the K_1 amplitude in this region may, however, not be resolved well on a 50 × 50 km grid. It will therefore be interesting to see the effect of a grid refinement.

Since the model performs well along the western and northern coast of Norway and in the Barents Sea it can be used for simulation of boundary input to high resolution models for limited area within this region. The capability of the model for driving small scale regional models will be exploited and results for the Haltenbanken area west of Norway have been reported by Nøst, 1988. A refined resolution version of the large scale model with grid size down to 25 × 25 km will also be tested.

8. Appendix

The equilibrium tide or the tide generating potential for the major tidal modes has been given by Schwiderski (1980a). We quote for the semi-diurnal tides

$$\bar{\eta} = K \cos^2 \phi \cos(\omega t + \chi + 2\theta), \tag{A.1}$$

and for the diurnal tides

$$\bar{\eta} = K \sin 2\phi \cos(\omega t + \chi + \theta), \tag{A.2}$$

where K is the amplitude of the partial equilibrium tide and χ is the astronomical argument relative to Greenwich midnight. (ϕ, θ) denote geographical latitude and longitude. For the semi-diurnal M_2 tide

$$K = 0.242334 \text{ m}, \quad \omega = 1.40519 \cdot 10^{-4} \text{ s}^{-1},$$

and for the diurnal K_1 tide

$$K = 0.141565 \text{ m}, \quad \omega = 0.72921 \cdot 10^{-4} \text{ s}^{-1}.$$

For simulation of charts of tidal amplitudes and phase lags relative to Greenwich which are not related to a particular point in time we may without loss of generality set the astronomical argument $\chi = 0$.

The components of the tide generating force $\partial\bar{\eta}/\partial x$ and $\partial\bar{\eta}/\partial y$ in a stereographic map projection can be easily derived albeit some tedious algebra. The equation of motion in a stereographic map projection (eqs. (2.6) and (2.8)) are obviously invariant for shift of origin and we conveniently take (x_p, y_p) as the coordinates of the pole. The geographical coordinates (ϕ, θ) for a point (x, y) are then given by the transformations

$$\tan(\theta - \theta_o) = \frac{y - y_p}{x - x_p}, \tag{A.3}$$

$$\tan^2\left(\frac{\pi}{4} - \frac{\phi}{2}\right) = \frac{(x - x_p)^2 + (y - y_p)^2}{p^2}, \tag{A.4}$$

where $p = a_s(1 + \sin\phi_s)R$ and θ_o is defined in

Section 2. The components of the tide generating force are

$$\frac{\partial \bar{\eta}}{\partial x} = \frac{\partial \bar{\eta}}{\partial \phi}\frac{\partial \phi}{\partial x} + \frac{\partial \bar{\eta}}{\partial \theta}\frac{\partial \theta}{\partial x},$$

$$\frac{\partial \bar{\eta}}{\partial y} = \frac{\partial \bar{\eta}}{\partial \phi}\frac{\partial \phi}{\partial y} + \frac{\partial \bar{\eta}}{\partial \theta}\frac{\partial \theta}{\partial y},$$

where the derivatives of ϕ and θ with respect to x and y are obtained from the coordinate transformation (A.3) and (A.4) and the derivatives of $\bar{\eta}$ are obtained from (A.1) and (A.2). By substitution we find

$$\frac{\partial \bar{\eta}}{\partial x} = A_1 \cos(\omega t + \chi) + A_2 \sin(\omega t + \chi), \qquad \text{(A.5)}$$

$$\frac{\partial \bar{\eta}}{\partial y} = B_1 \cos(\omega t + \chi) + B_2 \sin(\omega t + \chi). \qquad \text{(A.6)}$$

The coefficients A_1, A_2, B_1 and B_2 have the following expressions for the M_2 mode

$$A_1 = Q_M[\sin\phi \cos(\theta - \theta_o)\cos 2\theta + \sin(\theta - \theta_o)\sin 2\theta],$$

$$A_1 = -Q_M[\sin\phi \cos(\theta - \theta_o)\sin 2\theta - \sin(\theta - \theta_o)\cos 2\theta],$$

$$B_1 = Q_M[\sin\phi \sin(\theta - \theta_o)\cos 2\theta - \cos(\theta - \theta_o)\sin 2\theta],$$

$$B_2 = -Q_M[\sin\phi \sin(\theta - \theta_o)\sin 2\theta + \cos(\theta - \theta_o)\cos 2\theta],$$

where $Q_M = (2K/p)(1 + \sin\phi)\cos\phi$ and the value of K is given above. For the K_1 mode, we find

$$A_1 = -Q_K[\cos 2\phi \cos(\theta - \theta_o)\cos\theta - \sin\phi \sin(\theta - \theta_o)\sin\theta],$$

$$A_1 = Q_K[\cos 2\phi \cos(\theta - \theta_o)\sin\theta + \sin\phi \sin(\theta - \theta_o)\cos\theta],$$

$$B_1 = -Q_K[\cos 2\phi \sin(\theta - \theta_o)\cos\theta + \sin\phi \cos(\theta - \theta_o)\sin\theta],$$

$$B_2 = Q_K[\cos 2\phi \sin(\theta - \theta_o)\sin\theta - \sin\phi \cos(\theta - \theta_o)\cos\theta],$$

where $Q_K = (2K/p)(1 + \sin\phi)$.

Correction due to the elastic yielding of the earth can be allowed for by a uniform reduction of the amplitude of the equilibrium tide (Schwiderski, 1980a). We have included this effect in some simulation by simply reducing the value of the constant K with a factor 0.69.

9. Acknowledgements

This work has been supported by STATOIL, Stavanger, through contract T4257. We are grateful to members of the ocean modelling group at IOS, Bidston Observatory, Liverpool, UK for the benefit of many helpful discussions during the progress of the work. In particular we are indebted to R. A. Flather for providing us with data from his northeast Atlantic tidal model prior to publication. We also acknowledge valuable assistance from the staff at Norges Sjøkartverk, Stavanger, by providing data tapes with measured harmonic constants for tidal stations within the model area.

REFERENCES

Cartwright, D. E., Edden, A. C., Spencer, R. and Vassie, J. M. 1980. The tides of the northeast Atlantic Ocean. *Phil. Trans. Roy. Soc. London 298*, 87–139.

Cartwright, D. E. and Zetler, B. D. 1985. Pelagic tidal constants. *IAPSO Publication Scientifique No. 33.* Compiled by IAPSO Advisory committee on tides and mean sea level, 59 pp.

Davies, A. M. and Furnes, G. K. 1980. Observed and computed M_2 tidal currents in the North Sea. *J. Phys. Oceanogr. 10*, 237–257.

Davies, A. M. 1986. A three-dimensional model of the north west European continental shelf, with application to the M_4 tide. *J. Phys. Oceanogr. 16*, 797–813.

Flather, R. A. 1976. A tidal model for the north west European continental shelf. *Mém. Soc. Roy. Sci. Liége 6*, No. 10, 141–164.

Flather, R. A. 1981. Results from a model of the northeast Atlantic relating to the Norwegian coastal current. In *Norwegian Coastal Current Symposium*, Geilo, vol. II (eds. R. Sætre and M. Mork). University of Bergen, Norway, 31 pp.

Flather, R. A., Proctor, R. and Wolf, J. 1987. A tidal model for the northeast Atlantic. Personal communication.

Gjevik, B. 1988. Model simulations of tides and shelf waves along the shelves of the Norwegian–Greenland–Barents Seas. *Focus on modelling marine systems*, vol. 1, ed. A. M. Davies. CRC Press Inc, in press.

Gjevik, B. and Brembo, J. R. 1984. Numerical simulations of tidal oscillations in a rectangular basin with application to the tide in the Norwegian Sea. Report, April 1984, Dept. Math., University of Oslo, Norway, 75 pp.

Gjevik, B. and Straume, T. 1986. Model simulations of the M_2 and the K_1 tide in the Nordic Seas and the Arctic Ocean. Res. Report, Dept. Math., Univ. of Oslo, Norway, 55 pp.

Hansen, W. 1949. The semi diurnal tide in the North Atlantic Ocean. *Deutsche Hydr. Zeitsch. 2*, 44–51 (in German).

Hendershott, M. C. 1977. Numerical models of ocean tides. In *The Sea 6* (eds. E. D. Goldberg et al.). New York: Wiley Interscience, 47–95.

Huthnance, J. M. 1981. Large tidal currents near Bear Island and related tidal energy losses from the North Atlantic. *Deep Sea Res. 28A*, 51–70.

Kowalik, Z. and Untersteiner, N. 1978. A study of the M_2 tide in the Arctic Ocean. *Deutsche Hydr. Zeitsch. 31*, 216–229.

Kowalik, Z. 1979. A note on the co-oscillating M_2 tide in the Arctic Ocean. *Deutsche Hydr. Zeitsch. 32*, 100–112.

Kowalik, Z. 1981. A study of the M_2 tide in the ice-covered Arctic Ocean. *Modeling, Identification and Control 2*, No. 4, 201–223.

Martinsen, E. A., Gjevik, B. and Røed, L. P. 1979. A numerical model for long barotropic waves and strom surges along the western coast of Norway. *J. Phys. Oceanogr. 9*, 1126–1138.

Mathisen, J. P. and Johansen, Ø. 1983. A numerical tidal and storm surge model of the North Sea. *Marin Geodesy 6*, No. 3-4, 267–291.

Mesinger, F. and Arakawa, A. 1976. Numerical methods used in atmospheric models. *GARP Publ. Ser. WMO 17*, 64 pp.

Nekrasov, A. V. 1961. Preliminary charts of the main diurnal and semi-diurnal tidal waves in the Norwegian and the Greenland Seas. *Trans. Leningrad Hydrometeorol. Inst. 10*, No. 1, 81–87 (in Russian).

Nekrasov, A. V. 1962. Computation and construction of M_2 tidal charts in the Norwegian and Greenland Seas by the Hansen method. *Trudy Leningrad Gidrometeorol. Inst. 16*, 49–57 (in Russian).

Nøst, E. 1988. Model simulations of the M_2 tide in the Haltenbanken area. Report Dept. of Math., University of Oslo, Oslo, Norway (in Norwegian), 54 pp.

Schwiderski, E. W. 1979. Global ocean tides. Part II. The semi-diurnal principal lunar tide M_2. Atlas of tidal charts and maps. *Report 79-414*. Naval surface weapon center, Dahlgren, Va. USA, 90 pp.

Schwiderski, E. W. 1980a. On charting global ocean tides. *Rev. Geophys. and Space Physics 18*, 243–268.

Schwiderski, E. W. 1980b. Ocean tides. Part II. A hydrodynamical interpolation model. *Marin Geodesy 3*, 219–255.

Schwiderski, E. W. 1981. Global ocean tides. Part IV. The diurnal luni-solar declination tide (K_1). Atlas of tidal charts and maps. *Report 81-142*. Naval surface weapon center, Dahlgren, Va. USA, 80 pp.

Schwiderski, E. W. 1986. Tides. In *The Nordic Seas* (ed. B. G. Hurdle). New York: Springer-Verlag, 191–209.

Sverdrup, H. U. 1926. Dynamics of tides on the northern Siberian shelf. *Geophys. Publ. 4*, No. 5, Oslo, Norway, 76 pp.

Zahel, W. 1975. A global hydrodynamic–numerical 1°-model of the ocean tides: The oscillation system of the M_2-tide and its distribution of energy dissipation. *Ann. Geophys. 33*, 31–40.